ARTICLE

Controlling Supramolecular Chiral Nanostructures by Self-Assembly of a Biomimetic β-Sheet-Rich Amyloidogenic Peptide

Antoni Sánchez-Ferrer,[†] Jozef Adamcik,[†] Stephan Handschin,[†] Shu Hui Hiew,[‡] Ali Miserez,*[‡,§] and Raffaele Mezzenga*[†,‖]

[†]Department of Health Sciences & Technology, ETH Zurich, Zurich CH-8092, Switzerland
[‡]School of Materials Science and Engineering, Nanyang Technological University (NTU), 639798, Singapore
[§]School of Biological Sciences, NTU, 637551, Singapore
[‖]Department of Materials, ETH Zurich, Zurich CH-8093, Switzerland

Ⓢ Supporting Information

ABSTRACT: Squid sucker ring teeth (SRT) have emerged as a promising protein-only, thermoplastic biopolymer with an increasing number of biomedical and engineering applications demonstrated in recent years. SRT is a supra-molecular network whereby a flexible, amorphous matrix is mechanically reinforced by nanoconfined β-sheets. The building blocks for the SRT network are a family of suckerin proteins that share a common block copolymer architecture consisting of amorphous domains intervened by smaller, β-sheet forming modules. Recent studies have identified the peptide A1H1 (peptide sequence AATAVSHTTHHA) as one of the most abundant β-sheet forming domains within the suckerin protein family. However, we still have little understanding of the assembly mechanisms by which the A1H1 peptide may assemble into its functional load-bearing domains. In this study, we conduct a detailed self-assembly study of A1H1 and show that the peptide undergoes β-strands-driven elongation into amyloid-like fibrils with a rich polymorphism. The nanostructure of the fibrils was elucidated by small and wide-angle X-ray scattering (SAXS and WAXS) and atomic force microscopy (AFM). The presence of His-rich and Ala-rich segments results in an amphiphilic behavior and drives its assembly into fibrillar supramolecular chiral aggregates with helical ribbon configuration in solution, with the His-rich region exposed to the solvent molecules. Upon increase in concentration, the fibrils undergo gel formation, while preserving the same mesoscopic features. This complex phase behavior suggests that the repeat peptide modules of suckerins may be manipulated beyond their native biological environment to produce a wider variety of self-assembled amyloid-like nanostructures.

KEYWORDS: *self-assembly, peptide, SAXS, WAXS, AFM*
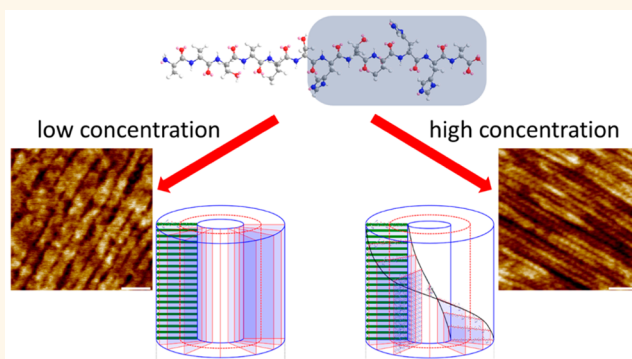
There has been increasing interest in the past decade toward development of peptide-based materials with controlled self-assembled structures for technological and biomedical applications.[1−4] Peptides and proteins can self-assemble and aggregate into mesoscopic materials and are widely found in the human body,[5,6] *e.g.*, blood fibrin,[7,8] collagen,[9,10] and actin[11,12] fibrils. Naturally occurring peptides self-assemble into conformationally stable regular secondary/tertiary structures controlled by their amino acid side chain residues, and they have inspired novel designed or biomimetic

peptide sequences for applications in biotechnology, biomineralization, bioelectronics, biosensing, and biomedicine, to name only a few.[13−20]

Special attention has been devoted to amphiphilic peptides, with surfactant-mimicking properties and bioactive functions, due to their tendency to generate ordered, self-assembled
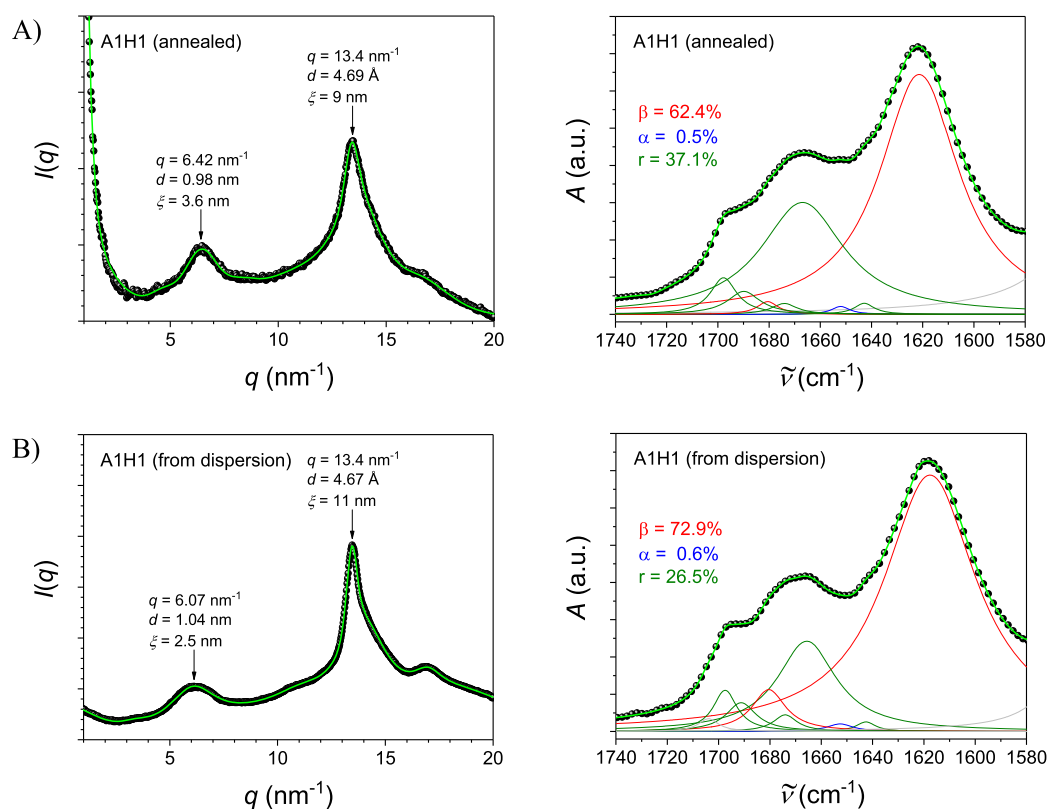
Figure 1. 1D WAXS intensity profile (left) and FTIR spectrum and peptide secondary structure population analysis (right) for (A) the annealed A1H1 sample at 120 °C under N_2 atmosphere and (B) the dried A1H1 sample from the 2 wt % dispersion. β, β-sheets; α, α-helices; r, random coils.

nanostructures for applications in drug delivery, tissue engineering, or smart hydrogels with a response triggered by changes in pH, light, ionic strength, and temperature.[21−28]

One of the most studied mesoscopic structures are β-sheet amyloid fibrils, peptide-based 1D nano-objects exhibiting cross-β-sheet structure, where the β-strands are arranged perpendicular to the fibril axis,[29] which are implicated and were discovered in the context of neurodegenerative diseases, such as Parkinson's, Alzheimer's, and Creutzfeldt−Jakob's.[30−32] Additionally, such fibrillar structures also show some physiological roles in living organisms, *e.g.*, fibrils production for cell adhesion, melanosomes development in mammalian, and peptide hormone storage in humans.[33−35] Nowadays, amyloid fibrils are increasingly used as templates for the development of nanotechnological materials in the production of biomembranes, biosensors, and energy conversion devices among other applications.[36−41]

Suckerins are a class of proteins identified in the sucker ring teeth (SRT) from Humboldt squids (*Dosidicus gigas*) with robust mechanical properties inferred due to the presence of amyloid-like β-sheet-rich regions.[42−46] Specifically, suckerins exhibit a block copolymer-like modular structure consisting of alanine (Ala)- and histidine (His)-rich modules (M1) intervened by longer Gly- and Tyr-rich modules (M2). Wide angle X-ray scattering (WAXS) studies have demonstrated a semicrystalline network in native SRT,[46] whereby M1 modules form nanoscale β-sheet regions within an amorphous matrix made of M2 modules. This structure is reminiscent of silk fibroins, with a major difference that the β-sheet (amyloid-like) domains in SRT are randomly oriented while they are preferentially oriented along the fiber axis in silk.[47] In addition,

small angle X-ray scattering (SAXS) investigations have shown that suckerins self-assemble into larger-scale fibrils packed into a hexagonal network, with temperature-dependent SAXS and WAXS indicating that β-sheets are stable up to 220 °C.[48] Recent solution NMR studies of model suckerins have confirmed that M1 modules adopt β-sheet conformation, whereas M2 modules are stabilized by $\pi−\pi$ stacking interactions of their aromatic residues.[49]

Recently, the **A1H1** sequence abundantly found in the suckerin protein family (peptide sequence AATAVSHTTHHA from M1 modules) has been studied in terms of self-assembly in water media. **A1H1** assembled into a highly compact crystal-like structure of β-sheets with intra- and inter-β-sheet distances of 4.4 and 5.4 Å, respectively,[50] which is more compact than the common distances observed in parallel or antiparallel β-sheet structures.[51−53] Moreover, due to its amphiphilic behavior, this peptide self-organizes hierarchically into long fibers composed of submillimeter bundles of micron-size fibrils formed by the association of *ca.* 10 nm width-long crystal-like β-sheet structures in water.

In this work, we show that the self-assembly behavior of the short peptidic sequence **A1H1** can be manipulated beyond the original self-assembly in water by using a less polar solvent media (acetonitrile/water azeotrope), which induces the formation of chiral hollow core−shell cylindrical objects due to the presence of a His-rich (polar and bulky, **H1**: HTTHHA) and Ala-rich (apolar and compact, **A1**: AATAVS) segments. Such long rod-like objects are fibrillar supramolecular chiral aggregates with helical ribbon configuration in solution, with the His-rich region exposed to the solvent molecules. Moreover, upon increase in concentration and over time, the
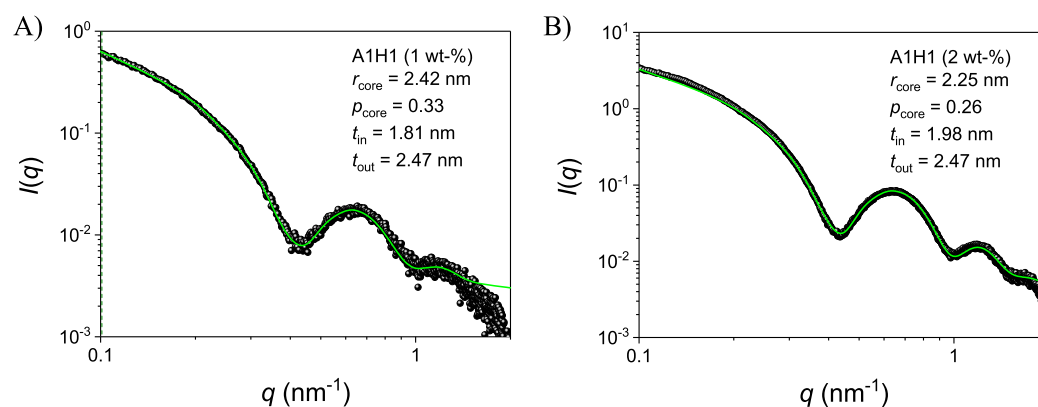
Figure 2. 1D SAXS intensity profile for A1H1 dispersions in acetonitrile/water at (A) 1 wt %, and (B) 2 wt %. Note: The green fitting curve corresponds to the form factor $P(q)$.

fibrils undergo gelation while preserving the same mesoscopic features.

RESULTS AND DISCUSSION

In order to understand the nature of the **A1H1** supramolecular aggregates in solution, we first studied the self-assembly behavior in the bulk state. A clear formation of β-sheet secondary structures was found, as revealed by the WAXS diffractogram after annealing the sample at 120 °C under N_2 atmosphere or after removal of the solvent under vacuum from the 2 wt % **A1H1** dispersion (Figures 1 and S2). In the following sections, "annealed samples" refer to solid samples, whereas "dispersions" refer to samples in the liquid state. A peak at q = 13.4 nm^{-1} ($d_{\beta\text{-strand}}$ = 4.7 Å) was found for both bulk samples, with correlation length values of $\xi_{\beta\text{-strand}}$ = 9−11 nm. The β-sheet spacing was evaluated from the peak at *ca.* q = 6.1 nm^{-1} ($d_{\beta\text{-sheet}}$ = 1.04 nm), with low correlation length values of $\xi_{\beta\text{-sheet}}$ = 3−4 nm. Moreover, FTIR analysis on both bulk samples showed enrichment of hydrogen bonded β-strand structures (from 60 to 70%), as confirmed by the strong β-sheet component of the amide I band at *ca.* 1620 cm^{-1} (Figures 1 and S3) corresponding to the C=O stretching vibrational mode.

SAXS and WAXS experiments were conducted on the 0.5, 1, and 2 wt % **A1H1** dispersions in the acetonitrile/water azeotrope in order to obtain information about the supramolecular structure of the β-strand rich self-assembled peptide. The 0.5 wt % **A1H1** dispersion did not show any clear SAXS pattern (Figure S4A), while the 1 and 2 wt % **A1H1** dispersions clearly showed a characteristic intensity profile (Figures 2A,B and S4B,C), with some degree of anisotropy for the latter. The WAXS intensity profile for such low concentrated samples (Figure S5) only indicated the presence of solvent with a characteristic broad peak at q = 17.2 nm^{-1} ($d_{solvent}$ = 3.7 Å). The 2 wt % **A1H1** dispersion exhibited birefringence. These properties were confirmed by the test tube-inversion method and by polarized light experiments (Figure S6), confirming the anisotropic colloidal nature of the peptidic nanostructures.

A1H1 dispersions were prepared and analyzed after 1 week by SAXS experiments. The 1D SAXS intensity profiles from the 1 and 2 wt % dispersions were fitted (Figure 2A,B) following the hollow poly core two-shells cylinder form factor $P(q)$ model (see SI) in order to extract the core radius and its polydispersity, and both the inner and outer shell thickness. This model could explain the presence of a hydrophilic (His-

rich) and a hydrophobic (Ala-rich) segment in the peptide sequence when self-assembled and dispersed in the acetonitrile/water azeotrope. The fitted scattering data resulted in a main core radius value of r_{core} = 2.25 nm (p_{core} = 0.26), and thicknesses of t_{in} = 1.98 nm and t_{out} = 2.47 nm were evaluated. These thickness values match well the distances obtained from molecular simulations where the fully stretched **A1H1** peptide has a length of 4.45 nm, and the His-rich segment (hydrophilic) has a length of 2.47 nm (Figure S1). The corresponding diameter of such cylindrical objects was $D_{dispersion}$ = 13.4 nm, calculated from the previous geometrical fitted parameters, with the peptide chains oriented perpendicular to the cylinder axis and distributed radially due to the formation of β-sheets.

As shown in Figure 2B, the 1D SAXS intensity profile of the 2 wt % **A1H1** dispersion shows a deviation from the experimental data at low q-values because of interactions between the rod-like objects, which is reflected by the presence of the structure factor $S(q)$. Such structure factor can be deduced from the anisotropic 2D pattern and the birefringence of the sample under polarized light. Thus, by dividing the 1D SAXS intensity profile $I(q)$ by the fitted form factor $P(q)$ at 2 wt %, hollow poly core two-shells cylinder model, the structure factor $S(q)$ could be obtained showing a maximum at *ca.* 46 nm, which could be attributed to the most probable nematic rod−rod distance of the **A1H1** hollow cylinders in the dispersion medium (Figure S7).

Further insight into the peptide self-assembly was gained by AFM experiments (Figures 3 and S8) upon depositing the three dispersions on mica. The 1 wt % **A1H1** dispersion was not birefringent (Figure S6), and the 2D SAXS pattern was fully anisotropic (Figure S4). This is not the case for the 2 wt % **A1H1** dispersion, which showed birefringence (domain sizes ranging from 400 to 800 nm) and anisotropy in the 2D SAXS experiments (presence of nematic field). The deposition on mica of the 2 wt % dispersion, or higher concentration, revealed a random distribution of nematic domains already existing in the bulk, which are transferred in full to the substrate. For the 1 wt % AFM sample, on the other hand, the first single long-rod object deposited on the surface induced side-packing of the next fibrils (Figure S9) with the corresponding local alignment only due to deposition. Therefore, there were no nematic domains for dispersions at concentration 1 wt %, or lower, in the bulk. In contrast, when deposited on mica the 1 wt % **A1H1** dispersion exhibited an
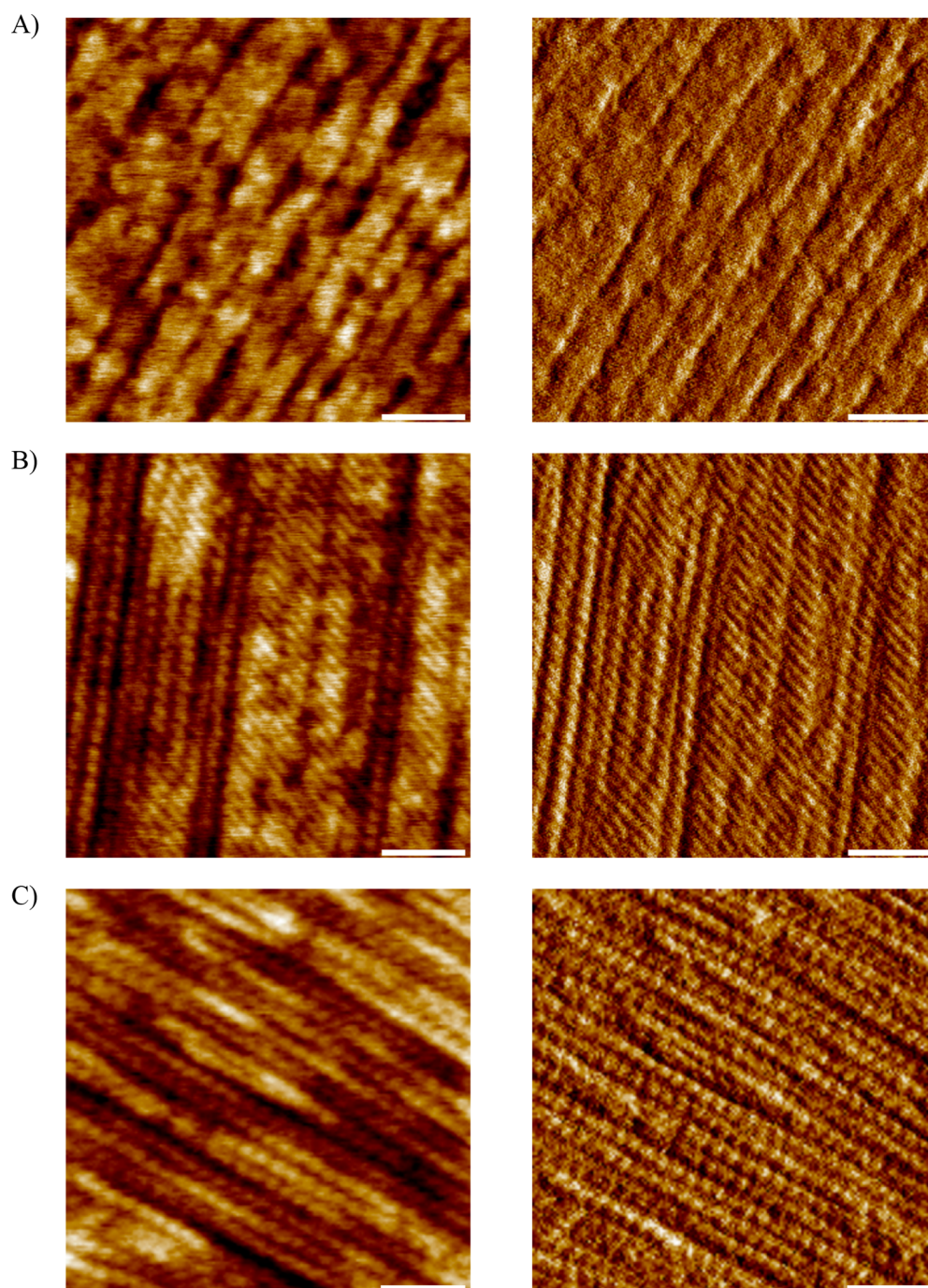
Figure 3. AFM height (left) and amplitude (right) profile image of the deposited (A) 1 wt %, (B) 2 wt %, and (C) 4 wt % A1H1 dispersion in acetonitrile/water. Note: Scale bar is 60 nm.

almost perfect alignment of the long rod-like objects in the scanned area.

Fast Fourier transform (FFT) of AFM images clearly indicated the presence of such anisotropic objects (Figure 4). The 360° azimuthally averaged intensities of the FFT signal (green curve) were plotted as single curves versus the reciprocal distance (q), along with averaged intensities measured over a circular sector of the FFT signal, where the anisotropic peaks appeared and were isolated from the averaged signal. The corresponding analysis indicated the presence of characteristic distances related to the rod-like object's features and fibril's internal periodicity. The interfibril

distance corresponded to the orthogonal signal to the fibril's axis (red curve), and the intrafibril distance to the internal periodic bands along the fibril axis (blue curve). For example, the image from the 1 wt % **A1H1** dispersion only contains information about the distance between the rod-like objects with a mean value of *ca.* 15 nm—the cross section AFM analysis indicated a local mean value of ca. 28 nm with a full width height maximum (fwhm) of 20 nm (Figure S10). The images from the 2 and 4 wt % **A1H1** dispersions also contain information about the observed tilted pattern obliques to the main fibril axis. The corresponding rod-to-rod distance and the distance between the tilted layers is 16 and 8.5 nm, and 15 and
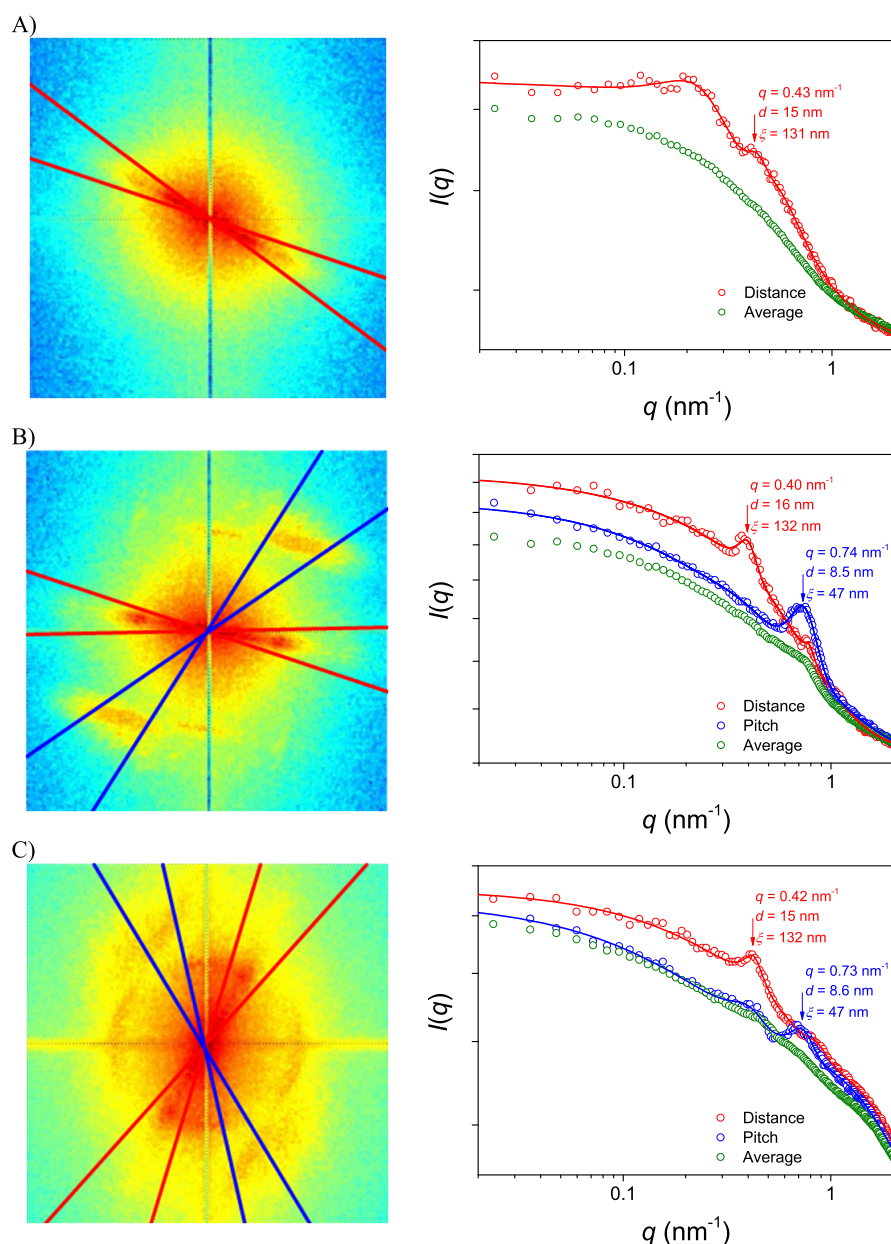
Figure 4. 2D (left) and 1D FFT plots (right) of the (A) 1 wt %, (B) 2 wt %, and (C) 4 wt % **A1H1** in acetonitrile/water from the AFM profile images in Figure 3. The red curve is the sector integration corresponding to the distance between the long rods, the blue curve is the sector integration corresponding to the pitch within the long rods, and the green curve is the 360° radial integration.

8.6 nm for the 2 and 4 wt % **A1H1** dispersions, respectively. The cross section AFM analysis showed a local mean value of ca. 15 nm with fwhm of 11 nm (Figure S10), where the average distance was calculated from the distance between maxima and the fwhm by deconvolution of the peaks, respectively. Measuring the tilt angle between both distance directions (48° for the 2 wt % **A1H1** dispersion and 53° for the 4 wt % **A1H1** dispersion) allowed the calculation of the tilt angle of the periodic bands with respect to the fibril axis and thus, the pitch of such fibrils which results to be ca. 11.4−11.6 nm.

These fibrillar structures arise from the coiling up of ribbons assembled from several β-sheets of the **A1H1** peptide, with its bulky His-rich domains exposed to the solvent molecules. Thus, the β-sheet planes appear radially distributed as "paddle wheels" and when the concentration of **A1H1** increases a

helical pitch appears due to axial sliding of β-sheets. The handedness of such helical structure, identified as left, has to be linked to the topology of the parallel β-strands (amino acid residues oriented perpendicular to the β-sheet plane) and demonstrates that supramolecular chirality assists the coiling of such ribbons.

Finally, after more than 3 months, the 2 wt % **A1H1** dispersion transformed into a dense gel material on the bottom of the flask, which could be manipulated by tweezers, and the supernatant solvent mixture remained on top of it. SAXS and WAXS experiments were performed on both the gel and the corresponding dried material (Figures 5A,B, S11, and S12). The SAXS intensity profile for the gel material showed a shift of the scattering intensity toward higher q-values, indicating that such hollow structures squeezed while keeping the thickness of the shell mostly identical (D_{gel} = 12.2 nm vs
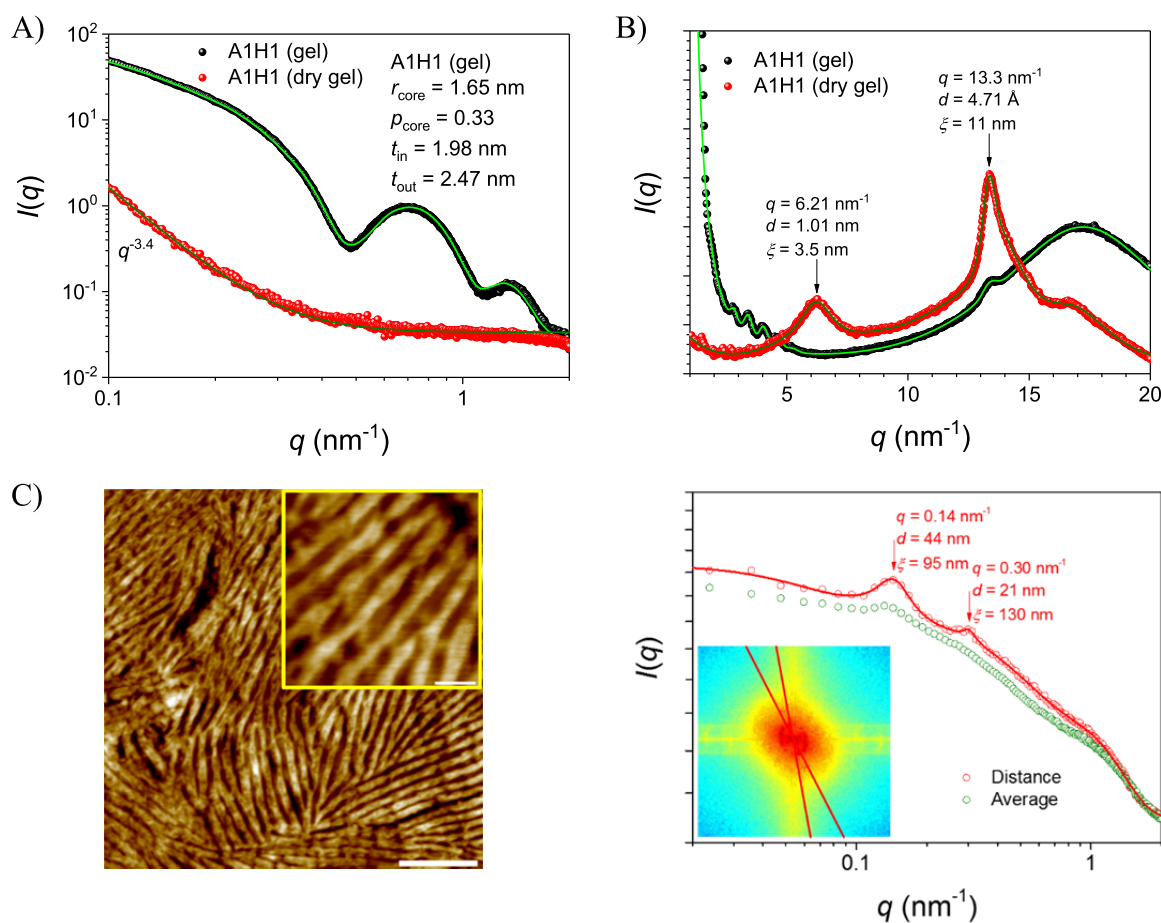
Figure 5. (A) 1D SAXS and (B) 1D WAXS intensity profile of the A1H1 gel (filled circles) in acetonitrile/water from the 2 wt % dispersion, and the corresponding dry gel (empty circles). (C) AFM height profile image (left) and FFT plot (right) of the dry gel. The red curve is the sector integration corresponding to the distance between the long rods, and the green curve is the 360° radial integration. Note: Scale bar is 300 nm; scale bar in the inset is 60 nm.

$D_{dispersion}$ = 13.4 nm; $r_{gel\text{-}core}$ = 1.65 nm vs $r_{dispersion\text{-}core}$ = 2.25 nm). These dimensional variations suggest desolvation from either the core of the cylindrical objects or during the formation of the 3D network, which can only hold a certain amount of solvent in the cages (syneresis). The WAXS intensity profile clearly indicated the presence of β-strands, as shown by the peak at q = 13.3 nm^{-1} ($d_{β\text{-}strand}$ = 4.7 Å) over the solvent peak at q = 17.2 nm^{-1} ($d_{solvent}$ = 3.7 Å). Upon drying the gel, the resulting transparent and brittle material showed no peaks in the SAXS region, while the common pattern for β-sheets in the WAXS region remained, confirming the presence of the β-sheet secondary structure of such self-assembled nanostructures.

AFM analysis was also carried out on the dry sample, which showed different types of long rigid objects (Figure S13). It seems that original long helical ribbons merged during gelation and/or upon drying, with the resulting objects becoming the building blocks for the formation of thicker microscopic bundles. The AFM analysis of such structures is better visualized in Figure 5C, where these long paired thin objects aligned into domains supporting the birefringent nature of the dried material (Figure S14). Analysis of the images showed the presence of such helical ribbons, which paired and twisted forming a bundle. FFT analysis indicated the presence of two peaks related to the pair-to-pair and to the rod-to-rod distance of ca. 44 and 21 nm, respectively, which is in agreement with

the cross section AFM analysis, i.e., local mean value of ca. 45–55 nm with a fwhm of 15–20 nm (Figure S15).

The formation of these supramolecular colloidal aggregates is caused by the self-assembly of the **A1H1** peptides by means of hydrogen bonding between the amide moieties from parallel peptide backbones, which form the characteristic β-sheet. Such a 2D hydrogen-bonded-rich flat structure interacts with other structures of the same nature. The presence of bulky histidine groups forces the β-sheet assembly to tilt, and thus the planes are not perfectly parallel, and a hollow cylinder can be formed. This is further supported by molecular dynamic simulations on these same peptides.[50] In this way, the His-rich segments are exposed to the solvent enhancing the dispersibility of the supramolecular object. The final nanostructure is concentration dependent: for dispersions 1 wt % or lower, smooth rod-like objects are observed, whereas for dispersions 2 wt % or higher, a pitch along the fiber axis appears due to axial sliding between the radially distributed β-sheet planes (see Figure S16). Such structural models are summarized in Figure 6. Moreover, the evolution of highly concentrated dispersions, e.g., 2 wt % or higher, yields solid-like materials that keep the same nanostructure of the precursor dispersions. Upon drying such gel materials, the helical objects pair to form bundles of two or more fibrils, which self-assemble into long and thicker rod-like objects capable of forming dense solids.
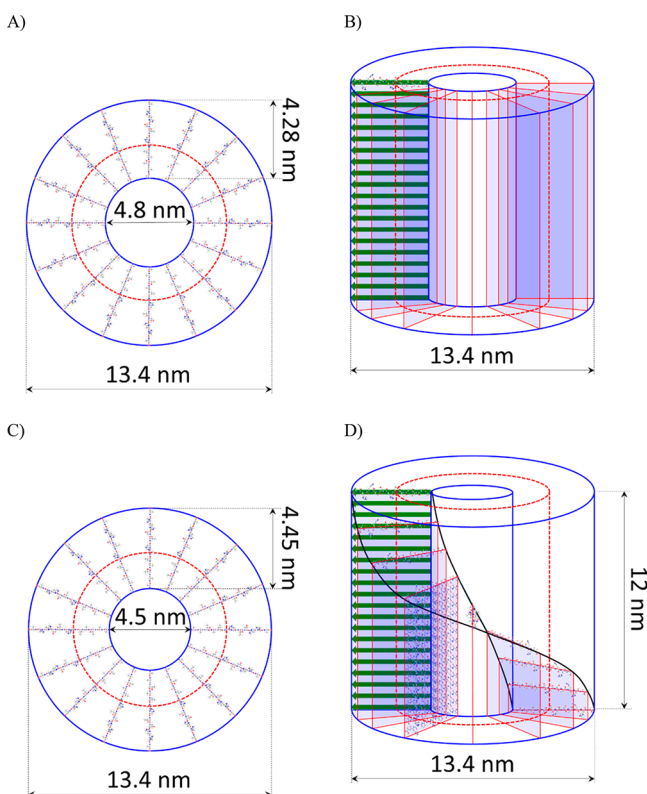
A)

4.28 nm

4.8 nm

13.4 nm

B)

13.4 nm

C)

4.45 nm

4.5 nm

13.4 nm

D)

12 nm

13.4 nm

Figure 6. Self-assembly of the 1 wt % **A1H1** (A) cross-section and (B) perspective of the hollow core-two-shell cylinder and 2 wt % **A1H1** (C) cross-section and (D) perspective of the hollow core-two-shell cylinder with helical pitch, in acetonitrile/water.

Examples of similar systems showing hollow cylinders have been described in the literature. For example, His-functionalized chiral peptide amphiphile (lauryl hexapeptide) assemblies underwent structural transitions from nanosheets to completely closed nanotubes upon increasing pH of the water media.[54] Equimolar mixtures of a positively charged peptide amphiphile (Lys-containing lauryl hexapeptide) with a negatively charged counter-partner (Glu-containing lauryl hexapeptide) formed twisted ribbons or nanotubes when Phe or Val amino acids were present in the peptide sequence, respectively.[55] In both cases, a similar radial distribution of β-sheets was proposed for the nanotube assemblies, where the hydrophobic lauryl tail is located in the inner part of the cylindrical shape exposing the bulky peptide residues to the water media. In a similar manner, a shorter peptide amphiphile (His-containing lauryl pentapeptide) containing a planar aromatic chromophore at the end of the hydrophobic part of the molecule formed nanofibers with a supramolecular chirality transferred from the chiral peptide to the π−π stacking core.[56]

A few additional comments are needed to explain the evolution of structural features upon removing the solvent of the different self-assembled objects in this work, *i.e.*, the dispersions, the gel, and the dry samples. **A1H1** dispersions (1 and 2 wt %) show scattering profiles in the small-angle region (Figures 2 and S4) but not in the wide-angle region where only the solvent signal was detected (Figure S5). Thus, this hollow cylindrical rod has a corona constituted by the self-assembly of β-sheets arranged in a radial orientation toward the central axis. The angular gradient and a low plane−plane correlation prevents the detection of the peaks at q = 6.2 and 13.4 nm^{-1}, *i.e.*, in the real space region spanned by the diverging plane−

plane interdistance across the corona. Once the **A1H1** gel is formed, the signals in both the small- and wide-angle regions become visible. The SAXS profile indicates the shrinkage of this hollow tube (Figures 5a and S11). As a result, the β-sheets come closer, with one of the characteristic peaks emerging at q = 13.4 nm^{-1} (Figures 5a and S12), corresponding to the interstrand distance in the β-sheet. A different scenario arises for the **A1H1** dry sample (annealed or after drying), where a precise scattering signal with the two characteristic peaks was observed in the wide-angle region (Figures 1A,B, 5B, S2, and S12), which corresponded to the expected inter β-sheet (1.0 nm) and inter β-strand (0.47 nm) distances. Collectively, these data support the idea that the weak and low β-sheet-correlated self-assembly of **A1H1** from the dispersions evolves toward the formation of denser structures after solvent removal, as indicated by the WAXS pattern and the FTIR spectrum of the dry system (Figures 1, S2, and S3). This is also consistent with the increased contrast to X-rays upon solvent removal, which can ingress the interplane space in the external region of the corona where spacing is sufficiently large to allow for solvation effects.

CONCLUSIONS

The self-assembly of the peptidic **A1H1**, an abundant peptide from the suckerin protein family forming squid SRT (peptide sequence AATAVSHTTHHA from M1 modules of suckerins), has been investigated in bulk and in dispersion. Depending on the concentration, the peptide sequence aggregates into β-sheets, in which the His-rich segments are exposed to the solvent molecules forcing a tilt between the β-sheet planes into a radial axisymmetric organization of fibrils with hollow cores. Upon increasing the concentration, such planes interact strongly and a shift between the planes along the fibril axis produces a nanostructural pitch of left-handedness. Finally, such chiral filaments form stable 3D networks, which partially expel the solvent from the inner core. Drying these solvent-containing systems yields compact materials formed by the interaction of long rigid filaments. These findings expand the understanding of self-assembling peptides with β-sheet forming propensity, the nature of their self-assembly under different conditions, such as concentration, solvent type, and solvent removal, and they also shed light on how supramolecular chirality ensues from the interplay among these factors. This study also shows that SRT-derived repeat peptides can be manipulated beyond their native biological environment to form a richer diversity of hierarchical structures. Owing to its amphiphilic nature, high aqueous solubility, and elevated His content, **A1H1** offers attractive potential as a nanoscale drug carrier with pH-dependent release governed by the protonation state of His. This feature can, for instance, be exploited to accelerate intracellular release of entrapped drugs because the release kinetics is faster at a weakly acidic pH corresponding to the endosomal pH, as demonstrated for a full-length suckerin.[57] Likewise, His-rich peptides have been exploited in gene transfection applications, with the key advantage of inducing nucleic acid release by the proton sponge effect.[58] Full-length suckerin/nucleic acid complexation was further enhanced by hydrophobic interactions with β-sheet domains,[57] and this mechanism should also be achievable with **A1H1** given its very high β-sheet content.

METHODS

Materials. Peptide synthesis was performed via Fmoc-chemistry solid-phase peptide synthesis on chlorotrityl chloride resin support as reported previously.[50] Peptide was purified with a reverse phase Agilent 300SB C-18 HPLC column on an Agilent Infinity 1260 to achieve >95% purity, and the molecular weight of the purified peptide was verified on a Thermo Finnigan LCQ Fleet LC/MS in ESI^+ mode. Figure S1 shows the chemical structure of the **A1H1** peptide together with both the end-to-end distance and the His-rich segment (hydrophilic) domain distance.

Techniques. Simultaneous SAXS and WAXS experiments were performed using a Rigaku MicroMax-002$^+$ microfocused beam (4 kW, 45 kV, 0.88 mA) in order to obtain direct information on the SAXS and WAXS reflections. The Cu Kα radiation ($\lambda_{CuK\alpha}$ = 1.5418 Å) was collimated by three pinhole (0.4, 0.3, and 0.8 mm) collimators. The scattered X-ray intensity was detected by a Fuji Film BASMS 2025 imaging plate system (15.2 × 15.2 cm^2, 50 μm resolution) and a two-dimensional Triton-200 X-ray detector (20 cm diameter, 200 μm resolution) for WAXS and SAXS regions, respectively. An effective scattering vector range of 0.1 nm^{-1} < q < 25 nm^{-1} was obtained, where q is the scattering wave vector defined as $q = 4\pi\sin\theta/\lambda_{CuK\alpha}$ with a scattering angle of 2θ.

Fourier-transform infrared (FTIR) spectra were obtained using a Varian 640 FTIR spectrometer equipped with a Specac Diamond ATR Golden Gate single attenuated total reflection (ATR) system. Samples were scanned at room temperature over the range of 4000−600 cm^{-1} with a resolution of 4 cm^{-1}, averaged over 64 scans, and baseline corrected. The amide I region was normalized, resolved by second-derivative analysis, and peak deconvoluted using Igor Pro 6.3.4.1 software.

Tapping mode atomic force microscopy (AFM) was carried out on a Multimode 8 Scanning Force Microscope (Bruker). Bruker AFM cantilevers for the tapping mode in soft tapping conditions were used at a vibrating frequency of 150 kHz. Images were simply flattened using the Nanoscope 8.1 software, and no further image processing was carried out. A 30 μL aliquot of solution at a certain concentration of **A1H1** was deposited onto freshly cleaved mica, incubated for 1 min, and dried with pressurized air.

Scanning Electron Cryomicroscopy (CryoSEM) images were obtained at −120 °C and 4 kV in a field emission SEM Leo Gemini 1530 (Carl Zeiss, Germany) equipped with a cold stage (VCT Cryostage, Bal-Tec/Leica). Three μL of liquid sample was placed on a glow discharged carbon coated 6 mm sapphire-disc (Rudolf Brügger SA, Switzerland). After manual plunge freezing in a mixture of liquid ethane/propane, the sample was freeze-dried up to −80 °C in a freeze-fracturing system BAF 060 (Bal-Tec/Leica, Vienna), coated with tungsten (1.5 nm at an elevation angle of 45°, and 1.5 nm at 90°).

Preparation of the Self-Assembled Structures. AFM and SAXS samples were prepared by dissolving 0.5, 1, 2, and 4 wt % of **A1H1** in the acetonitrile/water azeotrope (83.72% of acetonitrile and 16.28% water, which correspond to molar fractions of x_{ACN} = 0.69 and x_{H2O} = 0.31, respectively). For the SWAXS powder diffraction experiment, **A1H1** was prepared by solvent evaporation from the solutions or after annealing the sample as received from the synthesis at 120 °C under nitrogen atmosphere.

ASSOCIATED CONTENT

Ⓢ Supporting Information

The Supporting Information is available free of charge on the ACS Publications website at DOI: 10.1021/acsnano.8b03582.

Additional information about 2D and 1D SAXS and WAXS scattering profiles, FTIR spectra, AFM images and evaluations, optical and electron microscopy images, the chemical structure of **A1H1**, the form factor for a hollow poly core two-shell cylinder object, and the structure factor determination (PDF)

AUTHOR INFORMATION

Corresponding Authors
*E-mail: ali.miserez@ntu.edu.sg.
*E-mail: raffaele.mezzenga@hest.ethz.ch.

ORCID Ⓞ
Antoni Sánchez-Ferrer: 0000-0002-1041-0324
Ali Miserez: 0000-0003-0864-8170
Raffaele Mezzenga: 0000-0002-5739-2610

Notes
The authors declare no competing financial interest.

REFERENCES

(1) Deming, T. In *Peptide-Based Materials*; Springer-Verlag: Berlin, Heidelberg, 2012.
(2) Alemán, C.; Bianco, A.; Venanzi, M. In *Peptide Materials: from Nanostructures to Applications*; John Wiley & Sons, 2013.
(3) Shimanovich, U.; Efimov, I.; Mason, T. O.; Flagmeier, P.; Buell, A. K.; Gedanken, A.; Linse, S.; Akerfeldt, K. S.; Dobson, C. M.; Weitz, D. A.; Knowles, T. P. J. Protein Microgels from Amyloid Fibril Networks. *ACS Nano* **2015**, *9*, 43−51.
(4) Knowles, T. P. J.; Mezzenga, R. Amyloid Fibrils as Building Blocks for Natural and Artificial Functional Materials. *Adv. Mater.* **2016**, *28*, 6546−6561.
(5) Aguzzi, A.; O'Connor, T. Protein Aggregation Diseases: Pathogenicity and Therapeutic Perspectives. *Nat. Rev. Drug Discovery* **2010**, *9*, 237−248.
(6) Wei, G.; Su, Z.; Reynolds, N. P.; Arosio, P.; Hamley, I. W.; Gazit, E.; Mezzenga, R. Self-Assembling Peptide and Protein Amyloids: from Structure to Tailored Function in Nanotechnology. *Chem. Soc. Rev.* **2017**, *46*, 4661−4708.
(7) Ryan, E. A.; Mockros, L. F.; Weisel, J. W.; Lorand, L. Structural Origins of Fibrin Clot Rheology. *Biophys. J.* **1999**, *77*, 2813−2826.
(8) Undas, A.; Ariëns, R. A. Fibrin Clot Structure and Function: a Role in the Pathophysiology of Arterial and Venous Thromboembolic Diseases. *Arterioscler., Thromb., Vasc. Biol.* **2011**, *31*, e88−e99.
(9) Weber, K. T.; Sun, Y.; Tyagi, S. C.; Cleutjens, J. P. M. Collagen Network of the Myocardium: Function, Structural Remodeling and Regulatory Mechanisms. *J. Mol. Cell. Cardiol.* **1994**, *26*, 279−292.
(10) Cen, L.; Liu, W.; Cui, L.; Zhang, W.; Cao, Y. L. Collagen Tissue Engineering: Development of Novel Biomaterials and Applications. *Pediatr. Res.* **2008**, *63*, 492−496.
(11) Dominguez, R.; Holmes, K. C. Actin Structure and Function. *Annu. Rev. Biophys.* **2011**, *40*, 169−186.
(12) Reymann, A. C.; Boujemaa-Paterski, R.; Martiel, J. L.; Guerin, C.; Cao, W. X.; Chin, H. F.; de la Cruz, E. M.; Thery, M.; Blanchoin, L. Actin Network Architecture Can Determine Myosin Motor Activity. *Science* **2012**, *336*, 1310−1314.
(13) Löwik, D. W. P. M.; van Hest, J. C. M. Peptide-Based Amphiphiles. *Chem. Soc. Rev.* **2004**, *33*, 234−245.
(14) Fairman, R.; Åkerfeldt, K. S. Peptides as Novel Smart Materials. *Curr. Opin. Struct. Biol.* **2005**, *15*, 453−463.
(15) Pepe-Mooney, B. J.; Fairman, R. Peptides as Materials. *Curr. Opin. Struct. Biol.* **2009**, *19*, 483−494.
(16) Löwik, D. W. P. M.; Leunissen, E. H. P.; van den Heuvel, M.; Hansen, M. B.; van Hest, J. C. M. Stimulus Responsive Peptide-Based Materials. *Chem. Soc. Rev.* **2010**, *39*, 3394−3412.

(17) Boyle, A. L.; Woolfson, D. N. De Novo Designed Peptides for Biological Applications. *Chem. Soc. Rev.* **2011**, *40*, 4295−4306.

(18) Matson, J. B.; Zha, R. H.; Stupp, S. I. Peptide Self-Assembly for Crafting Functional Biological Materials. *Curr. Opin. Solid State Mater. Sci.* **2011**, *15*, 225−235.

(19) Matson, J. B.; Stupp, S. I. Self-Assembling Peptide Scaffolds for Regenerative Medicine. *Chem. Commun.* **2012**, *48*, 26−33.

(20) Ramakers, B. E. I.; van Hest, J. C. M.; Löwik, D. W. P. M. Molecular Tools for the Construction of Peptide-Based Materials. *Chem. Soc. Rev.* **2014**, *43*, 2743−2756.

(21) Stile, R. A.; Healy, K. E. Thermo-Responsive Peptide-Modified Hydrogels for Tissue Regeneration. *Biomacromolecules* **2001**, *2*, 185−194.

(22) Holowka, E. P.; Pochan, D. J.; Deming, T. J. Charged Polypeptide Vesicles with Controllable Diameter. *J. Am. Chem. Soc.* **2005**, *127*, 12423−12428.

(23) Carlsen, A.; Lecommandoux, S. Self-Assembly of Polypeptide-Based Block Copolymer Amphiphiles. *Curr. Opin. Colloid Interface Sci.* **2009**, *14*, 329−339.

(24) Cui, H.; Webber, M. J.; Stupp, S. I. Self-Assembly of Peptide Amphiphiles: from Molecules to Nanostructures to Biomaterials. *Biopolymers* **2010**, *94*, 1−18.

(25) Kotharangannagari, V. K.; Sánchez-Ferrer, A.; Ruokolainen, J.; Mezzenga, R. Photoresponsive Reversible Aggregation and Dissolution of Rod−Coil Polypeptide Diblock Copolymers. *Macromolecules* **2011**, *44*, 4569−4573.

(26) Kotharangannagari, V. K.; Sánchez-Ferrer, A.; Ruokolainen, J.; Mezzenga, R. Thermoreversible Gel−Sol Behavior of Rod−Coil−Rod Peptide-Based Triblock Copolymers. *Macromolecules* **2012**, *45*, 1982−1990.

(27) Sánchez-Ferrer, A.; Kotharangannagari, V. K.; Ruokolainen, J.; Mezzenga, R. Thermo-Responsive Peptide-Based Triblock Copolymer Hydrogels. *Soft Matter* **2013**, *9*, 4304−4311.

(28) Dehsorkhi, A.; Castelletto, V.; Hamley, I. W. Self-Assembling Amphiphilic Peptides. *J. Pept. Sci.* **2014**, *20*, 453−467.

(29) Dobson, C. M. Protein Folding and Misfolding. *Nature* **2003**, *426*, 884−890.

(30) Koo, E. H.; Lansbury, P. T.; Kelly, J. W. Amyloid Diseases: Abnormal Protein Aggregation in Neurodegeneration. *Proc. Natl. Acad. Sci. U. S. A.* **1999**, *96*, 9989−9990.

(31) Rambaran, R. N.; Serpell, L. C. Amyloid Fibrils: Abnormal Protein Assembly. *Prion* **2008**, *2*, 112−117.

(32) Knowles, T. P. J.; Vendruscolo, M.; Dobson, C. M. The Amyloid State and Its Association with Protein Misfolding Diseases. *Nat. Rev. Mol. Cell Biol.* **2014**, *15*, 384−396.

(33) Chapman, M. R.; Robinson, L. S.; Pinkner, J. S.; Roth, R.; Heuser, J.; Hammar, M.; Normark, S.; Hultgren, S. J. Role of Escherichia Coli Curli Operons in Directing Amyloid Fiber Formation. *Science* **2002**, *295*, 851−855.

(34) Fowler, D. M.; Koulov, A. V.; Alory-Jost, C.; Marks, M. S.; Balch, W. E.; Kelly, J. W. Functional Amyloid Formation within Mammalian Tissue. *PLoS Biol.* **2005**, *4*, e6.

(35) Maji, S. K.; Schubert, D.; Rivier, C.; Lee, S.; Rivier, J. E.; Riek, R. Amyloid as a Depot for the Formulation of Long-Acting Drugs. *PLoS Biol.* **2008**, *6*, e17.

(36) Cherny, I.; Gazit, E. Amyloids: Not Only Pathological Agents but also Ordered Nanomaterials. *Angew. Chem., Int. Ed.* **2008**, *47*, 4062−4069.

(37) Romero, D.; Aguilar, C.; Losick, R.; Kolter, R. Amyloid Fibers Provide Structural Integrity to Bacillus Subtilis Biofilms. *Proc. Natl. Acad. Sci. U. S. A.* **2010**, *107*, 2230−2234.

(38) Adler-Abramovich, L.; Aronov, D.; Beker, P.; Yevnin, M.; Stempler, S.; Buzhansky, L.; Rosenman, G.; Gazit, E. Self-Assembled Arrays of Peptide Nanotubes by Vapour Deposition. *Nat. Nanotechnol.* **2009**, *4*, 849−854.

(39) Hauser, C. A. E.; Maurer-Stroh, S.; Martins, I. C. Amyloid-Based Nanosensors and Nanodevices. *Chem. Soc. Rev.* **2014**, *43*, 5326−5345.

(40) Li, C. X.; Adamcik, J.; Mezzenga, R. Biodegradable Nanocomposites of Amyloid Fibrils and Graphene with Shape-Memory and Enzyme-Sensing Properties. *Nat. Nanotechnol.* **2012**, *7*, 421−427.

(41) Ryu, J.; Kim, S. W.; Kang, K.; Park, C. B. Mineralization of Self-Assembled Peptide Nanofibers for Rechargeable Lithium Ion Batteries. *Adv. Mater.* **2010**, *22*, 5537−5541.

(42) Miserez, A.; Weaver, J. C.; Pedersen, P. B.; Schneeberk, T.; Hanlon, R. T.; Kisailus, D.; Birkedal, H. Microstructural and Biochemical Characterization of the Nanoporous Sucker Rings from Dosidicus Gigas. *Adv. Mater.* **2009**, *21*, 401−406.

(43) Guerette, P. A.; Hoon, S.; Seow, Y.; Raida, M.; Masic, A.; Wong, F. T.; Ho, V. H.; Kong, K. W.; Demirel, M. C.; Pena-Francesch, A.; Amini, S.; Tay, G. Z.; Ding, D.; Miserez, A. Accelerating the Design of Biomimetic Materials by Integrating RNA-Seq with Proteomics and Materials Science. *Nat. Biotechnol.* **2013**, *31*, 908−915.

(44) Guerette, P. A.; Hoon, S.; Ding, D. W.; Amini, A.; Masic, A.; Ravi, V.; Venkatesh, B.; Weaver, J. C.; Miserez, A. Nanoconfined β-Sheets Mechanically Reinforce the Supra-Biomolecular Network of Robust Squid Sucker Ring Teeth. *ACS Nano* **2014**, *8*, 7170−7179.

(45) Hiew, S. H.; Guerette, P. A.; Zvarec, O. J.; Phillips, M.; Zhou, F.; Su, H.; Pervushin, K.; Orner, B. P.; Miserez, A. Modular Peptides from the Thermoplastic Squid Sucker Ring Teeth form Amyloid-like Cross-β Supramolecular Networks. *Acta Biomater.* **2016**, *46*, 41−54.

(46) Hiew, S. H.; Miserez, A. Squid Sucker Ring Teeth: Multiscale Structure−Property Relationships, Sequencing, and Protein Engineering of a Thermoplastic Biopolymer. *ACS Biomater. Sci. Eng.* **2017**, *3*, 680−693.

(47) Martel, A.; Burghammer, M.; Davies, R. J.; Di Cola, E.; Vendrely, C.; Riekel, C. Silk Fiber Assembly Studied by Synchrotron Radiation SAXS/WAXS and Raman Spectroscopy. *J. Am. Chem. Soc.* **2008**, *130*, 17070−17074.

(48) Latza, V.; Guerette, P. A.; Ding, D.; Amini, S.; Kumar, A.; Schmidt, I.; Keating, S.; Oxman, N.; Weaver, J. C.; Fratzl, P.; Miserez, A.; Masic, A. Multi-Scale Thermal Stability of a Hard Thermoplastic Protein-Based Material. *Nat. Commun.* **2015**, *6*, 1−8.

(49) Kumar, A.; Mohanram, H.; Kong, K. W.; Goh, R.; Hoon, S.; Lescar, J.; Miserez, A. Supramolecular Propensity of Suckerin Proteins Is Driven by β-Sheets and Aromatic Interactions as Revealed by Solution NMR. *Biomater. Sci.* **2018**, *21*, 401−408.

(50) Hiew, S. H.; Sánchez-Ferrer, A.; Amini, S.; Zhou, F.; Adamcik, J.; Guerette, P.; Su, H.; Mezzenga, R.; Miserez, A. Squid Suckerin Biomimetic Peptides Form Amyloid-like Crystals with Robust Mechanical Properties. *Biomacromolecules* **2017**, *18*, 4240.

(51) Kajava, A. V.; Squire, J. M.; Parry, D. A. Beta-Structures in Fibrous Proteins. *Adv. Protein Chem.* **2006**, *73*, 1−15.

(52) Hamley, I. W. Peptide Fibrillization. *Angew. Chem., Int. Ed.* **2007**, *46*, 8128−8147.

(53) Tycko, R.; Wickner, R. B. Molecular Structures of Amyloid and Prion Fibrils: Consensus versus Controversy. *Acc. Chem. Res.* **2013**, *46*, 1487−1496.

(54) Koc, M. H.; Ciftci, G. C.; Baday, S.; Castelletto, V.; Hamley, I. W.; Guler, M. O. Hierarchical Self-Assembly of Histidine-Functionalized Peptide Amphiphiles into Supramolecular Chiral Nanostructures. *Langmuir* **2017**, *33*, 7947−7956.

(55) Arslan, E.; Koc, M. H.; Uysal, O.; Dikecoglu, B.; Topal, A. E.; Garifullin, R.; Ozkan, A. D.; Dana, A.; Hermida-Merino, D.; Castelletto, V.; Edwards-Gayle, C.; Baday, S.; Hamley, I.; Tekinay, A. B.; Guler, M. O. Supramolecular Peptide Nanofiber Morphology Affects. *Biomacromolecules* **2017**, *18*, 3114−3130.

(56) Garifullin, R.; Guler, M. O. Supramolecular Chirality in Self-Assembled Peptide Amphiphile Nanostructures. *Chem. Commun.* **2015**, *51*, 12470−12473.

(57) Ping, Y.; Ding, D.; Ramos, R.; Mohanram, H.; Deepankumar, K.; Gao, J.; Tang, G.; Miserez, A. Supramolecular β-Sheets Stabilized Protein Nanocarriers for Drug Delivery and Gene Transfection. *ACS Nano* **2017**, *11*, 4528−4541.

(58) Midoux, P.; Pichon, C.; Yaouanc, J. J.; Jaffrès, P. A. Chemical Vectors for Gene Delivery: a Current Review on Polymers, Peptides

and Lipids Containing Histidine or Imidazole as Nucleic Acids Carriers. *Br. J. Pharmacol.* **2009**, *157*, 166−178.